

FeatureSLAM: Feature-enriched 3D gaussian splatting SLAM in real time

Christopher Thirgood¹, Oscar Mendez¹, Erin Ling¹, Jon Storey², Simon Hadfield¹
¹University of Surrey, ²I3D Robotics

{c.thirgood, o.mendez, chao.ling, s.hadfield}@surrey.ac.uk, jstorey@i3drobotics.com

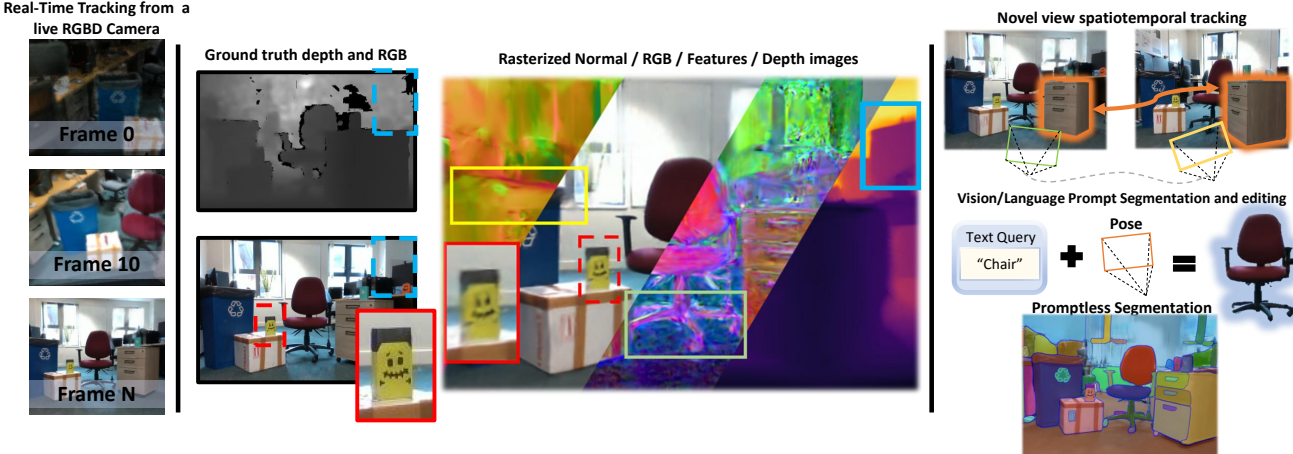


Figure 1. Overview of FeatureSLAM. Our real-time RGB-D SLAM framework integrates foundation model feature embeddings alongside geometry, producing high quality novel-view renderings from blurry live feeds. Left: The map is constructed online. Middle: Different map modalities visualized from a novel viewpoint in our custom live viewer. Right: Embedded features enable advanced manipulations (spatio-temporal semantic tracking, promptless segmentation, and language-guided segmentation).

Abstract

We present a real-time tracking SLAM system that unifies efficient camera tracking with photorealistic feature-enriched mapping using 3D Gaussian Splatting (3DGS). Our main contribution is integrating dense feature rasterization into the novel-view synthesis, aligned with a visual foundation model. This yields strong semantics, going beyond basic RGB-D input, aiding both tracking and mapping accuracy. Unlike previous semantic SLAM approaches (which embed pre-defined class labels) FeatureSLAM enables entirely new downstream tasks via free-viewpoint, open-set segmentation. Across standard benchmarks, our method achieves real-time tracking, on par with state-of-the-art systems while improving tracking stability and map fidelity without prohibitive compute. Quantitatively, we obtain 9% lower pose error and 8% higher mapping accuracy compared to recent fixed-set SLAM baselines. Our results confirm that real-time feature-enriched SLAM, is not only valuable for enabling new downstream applications. It also improves the performance of the underlying tracking and mapping subsystems, providing semantic and language masking results that are on-par with offline 3DGS models, alongside state-of-the-art tracking, depth and RGB rendering.

1. Introduction

Recent SLAM systems that embed novel view synthesis (NVS) models have achieved unprecedented map fidelity. However, they often incur prohibitive training times. Many NVS approaches, based on 3D Gaussian Splatting (3DGS) [19] or NeRF [33], require long offline training, which limits their applicability in real-world SLAM scenarios, which are predominantly online. Recent methods have extended coupled feature rasterization [53] into SLAM frameworks [16, 24, 56]. These systems demonstrate the potential of feature vector maps to improve semantic scene understanding and improve mapping convergence. However, they typically require hours of offline training, suffer from slow inference speed, and effectively convert a real-time SLAM problem into an offline process. Consequently, they have limited impact in robotics and real-world SLAM settings, where perception and mapping must operate online.

Recent vision foundation models such as SAM2 [40] offer fast, lightweight multi-scale feature extraction with strong generalization capabilities and significantly finer local and global feature granularity than prior works [9, 23, 39]. These features can be used for open-set segmentation, interactive annotation, and language-based prompting via integration with grounding models such as Grounding-

DINO [27, 41, 42]. Hierarchical feature representations remain underutilized in SLAM systems due to the difficulty of aligning dense multi-scale features with view-dependent rendering and varying feature scales.

In this work, we propose FeatureSLAM, a method for effectively embedding multi-level foundation model features into a real-time 3DGS-SLAM framework. This significantly improves model fidelity and tracking quality while operating online, without the extensive data preprocessing and masking of competing offline approaches. To the best of our knowledge, no existing system exploits multi-scale feature pyramids to enable rich open-set semantic understanding and interactive prompting, while operating in real-time.

In summary, our key contributions are:

1. A real-time online 3DGS-based SLAM framework that enables dense, open-set semantic mapping.
2. A feature-guided GICP tracking approach that leverages foundation-model feature maps and camera-plane rasterization instead of traditional depth supervision.
3. Tailored pruning, densification, and training strategies for compact feature-embedded 3DGS maps.

2. Related Work

2.1. Localization in SLAM

Early visual SLAM systems estimated camera motion and sparse landmarks using probabilistic filters, such as EKF-SLAM, or graph optimization frameworks [11, 30, 35]. While EKF-SLAM jointly updates both poses and landmarks, its $\mathcal{O}(n^2)$ complexity and fragile data association limit scalability. Graph-based approaches decouple motion and measurement updates, improving global consistency; however, they still rely heavily on repeatable point or line features, which degrade in texture-poor environments.

Learned pose graph optimizers [26] attempt to overcome these issues, but they still depend on robust feature tracking and often require extensive tuning. Geometry-based registration methods such as ICP [1] align raw sensor data directly. Variants including point-to-plane ICP [28], trimmed ICP [5], and Generalized ICP (GICP) [44] remain state-of-the-art for RGB-D and LiDAR odometry due to their speed and consistency. Minimalist pipelines like KISS-ICP [48] and its full SLAM extension KISS-SLAM [12] generalize well across sensors without per-scene tuning. However, all ICP-based methods require accurate geometric measurements; when depth is noisy or the field of view is narrow, tracking degrades and holes appear in reconstructed depth.

To increase robustness, several methods incorporate semantic cues. Techniques such as Semantic-EM ICP [36], SegICP [49], and SuMa++ [3] augment points with class probabilities to downweight ambiguous or dynamic regions. SAGE-ICP [7] extends this idea to real-time LiDAR segmentation. These approaches highlight that semantic consistency

is as critical as geometry for localization; however, they rely on preprocessed data and fixed semantic labels, which can become misaligned across frames, causing poor matching.

Inspired by this, we replace single-class labels with high-dimensional feature descriptors from open-set segmentation models such as SAM2 [40]. This yields viewpoint-stable features that are robust to lighting variation, occlusion, and clutter, while encoding richer semantics than traditional label-based segmentation.

2.2. Mapping in SLAM

Early dense SLAM systems such as KinectFusion [34], InfiniTAM [37], and BundleFusion [8] used truncated signed distance fields (TSDFs) to fuse depth into volumetric maps. These methods produced metrically accurate reconstructions but were memory-intensive and difficult to scale. Neural implicit representations emerged as an alternative. NeRF [33] and its SLAM adaptations (iMAP [47], NICE-SLAM [57], ESLAM [17], Point-SLAM [43]) replace TSDFs with MLP-based scene representations for photorealistic rendering. However, these models require per-frame backpropagation, are mostly offline, and render slowly, limiting real-world use. Hybrid solutions such as Orbeez-SLAM [6] and vMAP [22] decouple mapping from tracking using ORB-SLAM3 [2] for localization. However, loose coupling between map and tracker weakens the mutual feedback loop central to SLAM.

3D Gaussian Splatting. 3DGS is a modelling technique that represents scenes as explicit collections of anisotropic Gaussians. GS-SLAM [32] introduced monocular 3DGS based tracking, while SplatAM [18] improved photometric alignment using silhouette constraints at the cost of slower optimization. MonoGS [32] uses a gradient-based tracker on input RGB frames, and Photo-SLAM [15] incorporates ORB-SLAM3 for tracking. Yet, tracking often outpaces mapping, leading to inconsistencies, and both systems remain sensitive to hyperparameter tuning and texture-poor scenes. RGB-D GS-ICP [13] combines GICP tracking with Gaussian point positions. Although fast, it fails in self-similar or geometrically poor regions due to reliance on high-quality depth at every frame and suffers from drift.

Feature distilled 3DGS Recent work augments Gaussians with semantics for editing and open-vocabulary queries. Feature3DGS [53] embeds SAM [21] or LSeg [23] features but requires dense training and high-dimensional feature channels. LangSplat [38] uses language-conditioned features but with coarse boundaries due to low-dimensional embeddings. Approaches like GS-Grouping [51] and GaussianGrouping [51] extend SAM-based masks into 3D; GS-Grouping uses DEVA [4] to maintain temporal consistency. Methods such as NEDS SLAM [16], SemGauss-SLAM [55], and GS3 SLAM [24] jointly optimize appearance, seman-

tic features and the dense semantic label maps as a batch. However, these approaches are all offline, require extensive preprocessing, fixed-resolution features and slow rendering, resulting in inconsistent semantics and poor novel view synthesis quality.

In summary, existing 3DGS SLAM methods rely solely on photometric or geometric residuals for pose estimation and optimize semantics only during mapping, or treat semantics as view-invariant scalars, ignoring directional sensitivity. Our approach addresses both by embedding view-conditioned SAM2 descriptors into Gaussians and jointly optimizing semantic and geometric residuals in a unified, real-time pose optimization framework.

3. Preliminaries

3.1. 3DGS Rendering

In 3D Gaussian Splatting (3DGS), each Gaussian \mathcal{G}_i , is defined by its 3D position $\boldsymbol{\mu}_i \in \mathbb{R}^3$, covariance $\boldsymbol{\Sigma}_i \in \mathbb{R}^{3 \times 3}$, color $\mathbf{c}_i \in \mathbb{R}^3$, and opacity $\alpha_i \in [0, 1]$.

A pixel color C is computed via front-to-back alpha compositing of all Gaussians, sorted by depth:

$$C = \sum_{i=1}^N \mathbf{c}_i \alpha_i \prod_{j=1}^{i-1} (1 - \alpha_j) =: \sum_{i=1}^N \mathbf{c}_i \alpha_i \mathcal{T}_i, \quad (1)$$

where $\mathcal{T}_i = \prod_{j < i} (1 - \alpha_j)$ is the accumulated transmittance.

The opacity α_i for each Gaussian is modulated by its projected 2D footprint. Specifically,

$$\boldsymbol{\mu}_i^{2D} = \mathbf{K} \mathbf{P} \boldsymbol{\mu}_i, \quad \boldsymbol{\Sigma}_i^{2D} = \mathbf{J} \mathbf{R} \boldsymbol{\Sigma}_i \mathbf{R}^T \mathbf{J}^T, \quad (2)$$

where \mathbf{K} is the camera intrinsic matrix, \mathbf{P} is the world-to-camera projection matrix, \mathbf{R} is rotation, and \mathbf{J} is the Jacobian of the local affine approximation of the projection.

3.2. GICP Tracking

Generalized ICP (GICP) extends classical ICP by modeling each point as a Gaussian distribution, allowing local surface geometry to influence alignment via covariance estimation. We denote source (current frame) and target (global map):

$$G^s = \{(\boldsymbol{\mu}_i^s, \boldsymbol{\Sigma}_i^s)\}_{i=1}^N, \quad G^t = \{(\boldsymbol{\mu}_j^t, \boldsymbol{\Sigma}_j^t)\}_{j=1}^M.$$

Note that the colour and opacity parameters of the 3DGS model are omitted from this process.

Correspondence and Gaussian error model For each source Gaussian, we define the process π to find the nearest neighbor in the target set:

$$\pi(i) = \arg \min_j \|\boldsymbol{\mu}_i^s - \boldsymbol{\mu}_j^t\|_2.$$

Given this correspondence, under a rigid-body transform $T = (\mathbf{R}, \mathbf{t}) \in SE(3)$,

$$\boldsymbol{\mu}_i^s \mapsto \mathbf{R} \boldsymbol{\mu}_i^s + \mathbf{t}, \quad \boldsymbol{\Sigma}_i^s \mapsto \mathbf{R} \boldsymbol{\Sigma}_i^s \mathbf{R}^T.$$

The residual is thus,

$$\mathbf{d}_i = \boldsymbol{\mu}_{\pi(i)}^t - (\mathbf{R} \boldsymbol{\mu}_i^s + \mathbf{t}).$$

Because both points are Gaussian-distributed,

$$\mathbf{d}_i \sim \mathcal{N}(\mathbf{0}, \boldsymbol{\Sigma}_{\pi(i)}^t + \mathbf{R} \boldsymbol{\Sigma}_i^s \mathbf{R}^T).$$

Maximum-likelihood pose estimation. The optimal pose minimizes the sum of Mahalanobis distances:

$$T^* = \arg \min_{\mathbf{R}, \mathbf{t}} \sum_{i=1}^N \mathbf{d}_i^\top (\boldsymbol{\Sigma}_{\pi(i)}^t + \mathbf{R} \boldsymbol{\Sigma}_i^s \mathbf{R}^T)^{-1} \mathbf{d}_i.$$

This non-linear least-squares problem is solved iteratively using a Lie algebra parameterization of $SE(3)$ and Gauss–Newton or Levenberg–Marquardt optimization.

4. Methodology

Our approach enables real-time, high-resolution, feature-distilled mapping within a 3D Gaussian Splatting (3DGS) framework, facilitating semantic understanding for robotics and AR applications. As shown in Fig. 2, our pipeline consists of three main components: Image feature extraction, Feature guided GICP and feature distilled 3DGS mapping.

4.1. Online Feature Rasterization

Feature distillation from foundation models into offline 3DGS has recently been shown to improve not only visual fidelity but also geometric understanding, as image encoders provide denoised, semantically rich signals that regularize view synthesis. However, all prior works rely on slower ViT/DINO-style backbones, forcing a trade-off between accuracy and throughput and precluding real-time online SLAM systems. We instead adopt the hierarchical feature pyramid from SAM2’s Hierarchical encoder, which delivers multi-scale descriptors at real-time speed. Beyond efficiency, its pyramid captures complementary context (fine edges at high resolution and semantics at coarse resolution). Embedding these features in the Gaussians and decoding them jointly supplies the renderer with implicit scene priors while retaining low latency for online SLAM.

For each RGB–D frame, our encoder produces feature maps with different channel depths (256, 64 and 32) and spatial resolutions (64x64, 128x128 and 256x256, respectively), $\{F^{(\ell)}\}_{\ell \in \{4, 8, 16\}}$. We bilinearly up-sample at the projected Gaussian mean \mathbf{x}_i and concatenate the 3 feature maps to form u_i . A joint encoder ϕ compresses u_i into a compact latent space, $f_i = \phi(u_i)$, removing redundancies between the feature maps. Corresponding lightweight heads $\phi^{(\ell)}$ are trained to decode back to each of the 3 feature maps. Finally, we augment each Gaussian \mathcal{G}_i in the 3DGS model with these compact feature embeddings $f_i \in \mathbb{R}^D$.

To ensure efficient online performance, our feature autoencoder is pretrained on unrelated datasets (COCO and

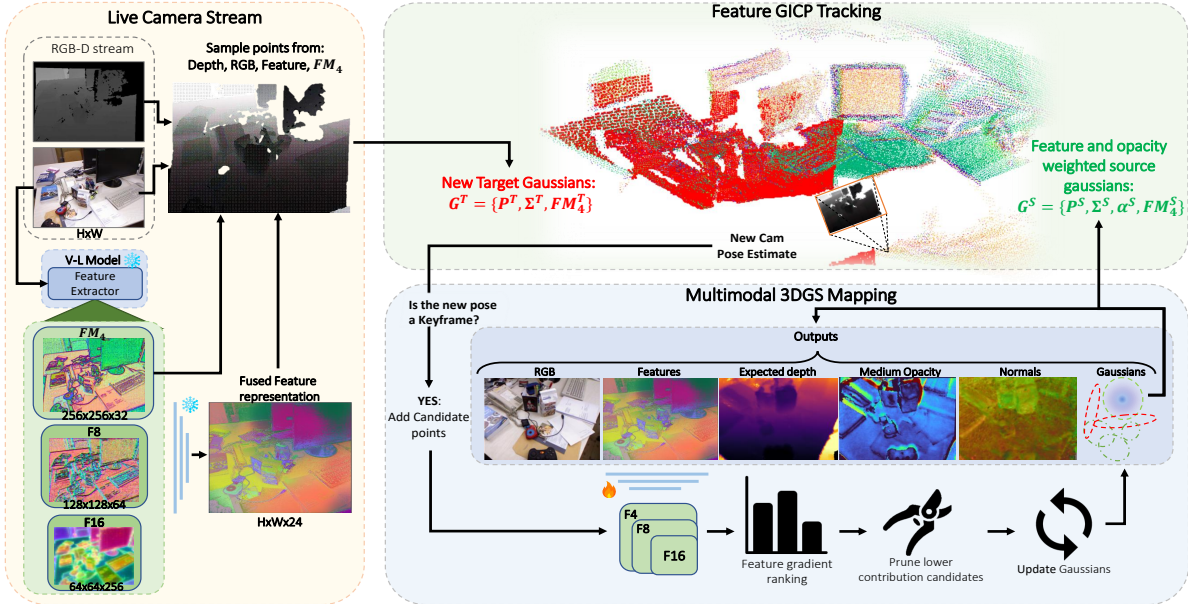


Figure 2. FeatureSLAM overview, including the feature extraction, tracking and mapping modules.

scannet). To preserve this pretraining and enable efficient adaptation at runtime, we insert LoRA blocks between each head of the decoder. These LoRA blocks are frozen as zero-convolutions during pretraining. Then, during online SLAM, the main body of the autoencoder is frozen and only the LoRA blocks are unfrozen (with a gradual warmup of the learning rate). We find this approach prevents catastrophic forgetting during the online training of the autoencoder, while allowing adaptation of the learned latent-space to account for the unique artifacts induced by volumetric rendering.

4.2. Robust Depth Rasterization.

Depth supervision is essential in 3DGS-based SLAM to suppress floating Gaussians and maintain geometric consistency. Existing systems estimate depth either as the expected value along the ray, modulated by transmittance,

$$D_{\text{exp}}(\mathbf{x}) = \sum_i \mathcal{T}_i(\mathbf{x}) \alpha_i(\mathbf{x}) z_i, \quad (3)$$

or by projecting depth sensor values to each Gaussian, as in GS-ICP-SLAM [13]. Both assume a *single* depth value per Gaussian and per ray. This breaks down near surface discontinuities or slanted planes, and introduces a strong dependency on the accuracy and completeness of the depth sensor measurements. These techniques tend to work well on synthetic data with perfect ground-truth depth, but can be unreliable for real-world operation.

Instead, we propose using structure-aware depth rasterization, where individual Gaussians induce different depths at all overlapping pixels, based on their shape and orientation.

More formally, we show that under perspective projection, a 3D Gaussian produces a *locally planar depth field* over its projected ellipse.

Following [52], we note that for a target pixel \mathbf{x} with a corresponding ray vector $\hat{\mathbf{r}}$ we can define the maximum likelihood intersection with Gaussian \mathcal{G}_i (μ_i and Σ_i) as

$$t^* = \arg \max_t \exp\left(-\frac{1}{2} (\hat{\mathbf{r}} - \mu_i)^\top \Sigma_i^{-1} (\hat{\mathbf{r}} - \mu_i)\right), \quad (4)$$

where t^* is the depth along the ray corresponding to the maximum density of \mathcal{G}_i . This yields a closed-form solution $t^* = \hat{\mathbf{r}}^\top \mathbf{q}_i$ in ray-space, where

$$\mathbf{q}_i = \frac{\Sigma_i^{-1} \mu_i}{\mu_i^\top \Sigma_i^{-1} \mu_i}. \quad (5)$$

After perspective division and first-order expansion around μ_i^{2D} , the Gaussian induces a planar depth field:

$$D_i(\mathbf{x}) = \beta_i^\top \begin{bmatrix} \mathbf{x} - \mu_i^{2D} \\ 1 \end{bmatrix}, \quad \beta_i = [a_i, b_i, \mu_{i,z}]^\top, \quad (6)$$

where (a_i, b_i) are determined analytically from Σ_i , μ_i and the camera intrinsics. Thus, depth varies linearly over the Gaussian's 2D footprint, rather than remaining constant. Integrating this local per-Gaussian variation into the depth rasterization of eq. 3, we obtain

$$D_{\text{exp}}(\mathbf{x}) = \sum_i \mathcal{T}_i(\mathbf{x}) \alpha_i(\mathbf{x}) D_i(\mathbf{x}). \quad (7)$$

This camera-plane depth formulation eliminates the far-plane bias of GS-ICP-SLAM, preserves slanted surfaces,

produces sharper silhouettes, and yields stable depth and normal gradients for optimization.

To additionally reduce bias from semi-transparent regions, we also compute the *median* depth $D_{\text{med}}(\mathbf{x})$ by finding the depth at which accumulated opacity first exceeds 0.5 along the ray. These are complementary: expected depth is smooth but biased; median depth preserves sharp edges.

4.3. Depth-normal consistency & regularization

To fully exploit the camera-plane depth model, we impose losses that enforce local depth structure, surface consistency, and well-conditioned Gaussian geometry.

First, instead of supervising depth with only an ℓ_1 loss, we include a patch-wise Pearson correlation loss (PCC). Given rendered depth D and ground-truth depth D^{obs} , we divide the image into $p \times p$ blocks and compute

$$\mathcal{L}_{\text{pcc}} = 1 - \rho(D, D^{\text{obs}}),$$

where ρ is the zero-mean, normalized cross-correlation within each block. This loss is invariant to absolute scale or bias and focuses on preserving relative depth variations (slanted planes, discontinuities, and local surface shape). This makes it especially effective in regions where Gaussian blending or transmittance leaves depth slightly biased but structurally correct.

Second, to measure surface smoothness, we derive surface normals from two complementary depth signals (expected camera plane depth and median depth) as well as from the depth sensor input (D_{obs}). These are estimated via finite differences

$$\mathbf{n}_{\text{exp}} = \frac{\partial_u D_{\text{exp}} \times \partial_v D_{\text{exp}}}{\|\partial_u D_{\text{exp}} \times \partial_v D_{\text{exp}}\|}, \quad (8)$$

$$\mathbf{n}_{\text{med}} = \frac{\partial_u D_{\text{med}} \times \partial_v D_{\text{med}}}{\|\partial_u D_{\text{med}} \times \partial_v D_{\text{med}}\|}, \quad (9)$$

$$\mathbf{n}_{\text{obs}} = \frac{\partial_u D_{\text{obs}} \times \partial_v D_{\text{obs}}}{\|\partial_u D_{\text{obs}} \times \partial_v D_{\text{obs}}\|}. \quad (10)$$

We then introduce cosine similarity losses between each pair of normal vectors. This encourages the depth field to form coherent planes and sharp edges, suppressing floaters and improving photometric alignment.

During online mapping, many Gaussians are initialized from noisy stereo or depth measurements and then rapidly optimized by photometric and feature losses. Without additional constraints, their covariance matrices often collapse into needle-like shapes (rank ≈ 1), especially along viewing rays. This is visible in the visual results shown in Fig. 3. This causes unstable normals, overconfident depth, and poor alignment with the true surface tangent plane, ultimately harming tracking and pruning. This is exacerbated in real-world deployment, where missing regions of the depth map can induce sharp gradients along their borders.

To counteract this, we adopt a ranking barrier. Given a Gaussian with scaling vector $\mathbf{s}_i = [s_{i,x}, s_{i,y}, s_{i,z}]$, we compute normalized singular values:

$$p_{i,k} = \frac{s_{i,k}^2}{\sum_{j \in \{x,y,z\}} s_{i,j}^2}, \quad k \in \{x, y, z\},$$

and define the entropy of the scale distribution,

$$H_i = - \sum_{k \in \{x,y,z\}} p_{i,k} \log(p_{i,k}),$$

We then define $\text{erank}(\Sigma_i)$ as $\exp(H_i) \in [1, 3]$, where $\text{erank} \approx 1$ indicates a degenerate needle-shaped Gaussian, and $\text{erank} \approx 3$ indicates an isotropic Gaussian.

We then impose the barrier loss:

$$\mathcal{L}_{\text{erank}} = \lambda_e \left[-\log(\text{erank}(\Sigma_i) - 1 + \epsilon) \right],$$

which encourages Gaussians to have an $\text{erank} > 1$, preventing collapse to 1D structures. To avoid over-regularizing Gaussians early in SLAM, λ_e is ramped from a small initial value λ_0 to λ_{max} over the first T iterations:

$$\lambda_e(t) = \lambda_0 + (\lambda_{\text{max}} - \lambda_0)(1 - e^{-t/T}).$$

A second common mode of Gaussian collapse, which is not strongly discouraged by the above loss, is for the Gaussians to become extremely flat and disc-shaped (i.e. $s_z \ll s_x, s_y$). We therefore include a thinness penalty:

$$\mathcal{L}_{\text{thin}} = \lambda_{\text{thin}} \cdot \mathbb{E}_i [s_{i,3}^{\downarrow}],$$

where $s_{i,3}^{\downarrow}$ is the smallest scale after sorting (s_x, s_y, s_z) . This encourages a minimum Gaussian volume, preventing zero-width planar splats that are overly confident in their depth, interfering with GICP tracking or depth rendering.

Combined, the PCC depth loss, depth-normal consistency, and eRank regularization align the geometry with real surfaces, reduce drift and floater artifacts, and provide cleaner gradients for joint online mapping and tracking.

4.4. Per-splat backward parallelization

To sustain real-time optimization, we adopt the per-splat backward pass strategy introduced in Taming3DGS [29]. Instead of assigning one thread per pixel (which causes heavy atomic contention during gradient accumulation), each warp iterates over splats and locally reconstructs transmittance values using precomputed checkpoints T^* across subrange intervals of P Gaussians:

$$T_{kP}^* = T_{k(P-1)}^* \prod_{m=k(P-1)}^{kP-1} (1 - \alpha_m),$$

with the per Gaussian transmittance being recovered as

$$\mathcal{T}_i = \mathcal{T}_{\lfloor i/P \rfloor P}^* \prod_{m=\lfloor i/P \rfloor P}^{i-1} (1 - \alpha_m).$$

This guarantees an *exact* recovery of the original transmittance, while completely avoiding atomic operations in the backward pass.

Practically, this yields a speedup in gradient computation, enabling more inner-loop gradient steps per GICP pose update [10]. However, we observe a subtle trade-off: faster photometric convergence can cause Gaussians to overfit to local color/feature residuals, drifting away from the geometry implied by the initial GICP covariance estimates. When the rendering model over-optimizes between pose updates, the accumulated error manifests as increased camera drift. As a result, while per-splat backward parallelization improves computational throughput, we cap the number of gradient steps per frame to preserve tracking stability.

4.5. Modelling Losses

We supervise our modelling with a range of data-driven losses on the appearance, depth, normals, and features,

$$\begin{aligned} \mathcal{L}_{\text{rgb}} &= \lambda_1 \|C - C^{\text{obs}}\|_1 + \lambda_2 (1 - \text{SSIM}(C, C^{\text{obs}})), \\ \mathcal{L}_{\text{feat}} &= \lambda_f \|\hat{F} - F^{\text{obs}}\|_1, \\ \mathcal{L}_{\text{depth}} &= \lambda_d \|D - D^{\text{obs}}\|_1 + \lambda_{\text{pcc}} (1 - \rho_{\text{PCC}}^{(p)}(D, D^{\text{obs}})), \\ \mathcal{L}_{\text{nrm}} &= \lambda_n [(1 - \cos \angle(\mathbf{n}_{\text{exp}}, \mathbf{n}_{\text{obs}})) + (1 - \cos \angle(\mathbf{n}_{\text{med}}, \mathbf{n}_{\text{obs}}))] \end{aligned}$$

where $\rho_{\text{PCC}}^{(p)}$ is a patchwise Pearson correlation (avg-pooled using blocks of size p), \mathbf{n}_{exp} and \mathbf{n}_{med} are rendered normals from expected and median depth, and \mathbf{n}_{obs} is the normals from the depth sensor. We also include the eRank barrier and “thin” regularizer to discourage needle-like or disc-like Gaussians while stabilizing scales. This leads to our overall reconstruction loss,

$$\mathcal{L} = \mathcal{L}_{\text{rgb}} + \mathcal{L}_{\text{feat}} + \mathcal{L}_{\text{depth}} + \mathcal{L}_{\text{nrm}} + \mathcal{L}_{\text{erank}}.$$

4.6. Feature GICP tracking

Classical GICP (as detailed in Sec. 3.2) aligns two point sets by minimizing a Mahalanobis distance between geometrically corresponding Gaussians. While effective on dense, noise-free depth scans, it becomes unstable in RGB-D SLAM where large texture-less regions, specular surfaces, or depth holes lead to ambiguous geometry.

We also note a systemic discrepancy between ICP-based tracking (where every point represents a geometry measurement) and 3DGS modelling (where the geometry is aggregated across many points via volumetric rendering). For example, it is common in 3DGS that the appearance of a single point on a complex surface might be formed through

the composition of many co-located Gaussians. However, the incoming depth sensor will only produce a single point measurement at that position.

To resolve these issues, we first note that in FeatureSLAM, both our model and observations also incorporate dense, view-stable semantic information, which can help resolve misalignments. We also note that the per-Gaussian opacities can act as a proxy for the level of volumetric composition that is likely happening at a particular point. This allows us to propose a refined Tracking formulation, which is modulated to account for Gaussian visibility and semantic matching score

$$T^* = \arg \min_{\mathbf{R}, \mathbf{t}} \sum_{i=1}^N \alpha_i (\mathbf{d}_i^\top (\Sigma_{\pi(i)}^t + \mathbf{R} \Sigma_i^s \mathbf{R}^T)^{-1} \mathbf{d}_i + d_f),$$

where $(i, \pi(i))$ is the geometric correspondence, and

$$d_f = \exp(-\gamma \|\mathbf{f}_i^s - \mathbf{f}_{\pi(i)}^t\|_2^2).$$

As in standard GICP, we linearize on $\mathfrak{se}(3)$ and solve with Gauss–Newton.

4.7. Keyframe Selection

To maintain both computational efficiency and map consistency, a new keyframe is inserted only when the current camera pose deviates sufficiently from the last keyframe in either translation or rotation, or when the tracking uncertainty exceeds a predefined threshold. In particular, let T_k denote the last keyframe pose and T_c the current pose estimate. A keyframe is created when:

$$\|\mathbf{t}_c - \mathbf{t}_k\| > \tau_t \quad \text{or} \quad \angle(\mathbf{R}_c \mathbf{R}_k^\top) > \tau_r \quad \text{or} \quad \sigma_{\text{gicp}} > \tau_\sigma,$$

where τ_t and τ_r are translational and rotational motion thresholds (e.g. 5 cm and 3°), and τ_σ is the root-mean-square GICP residual indicating pose uncertainty. Tracking frames contribute only to pose refinement and do not expand the 3DGS model, while keyframes are used to insert new Gaussians into the map and trigger model refinement. This balances accuracy and runtime, ensuring new geometry is fused only when it provides robust, genuinely novel viewpoints.

4.8. Semantic gradient-based pruning & refinement

Foundation model features greatly enhance geometry and visual fidelity in 3DGS, but they also inflate the memory footprint and slow optimization due to their high-dimensionality. Moreover, our Feature–GICP tracking continuously inserts new Gaussians from every keyframe’s observations. Without regulation, the number of splats grows without bounds, quickly degrading rendering time and SLAM performance.

To maintain a compact but semantically meaningful scene representation, we adopt an enhanced pruning strategy via the gradient-based impact of new Gaussians on the

model semantics. We refer to this process of entering new Gaussians into the 3DGS model as a ‘refinement round’.

For each Gaussian \mathcal{G}_i , we define an importance score:

$$\psi_i = \sum_{x \in \Omega_i} \left| \frac{\partial \mathcal{L}_{\text{rgb}}}{\partial \alpha_i(x)} \right|,$$

where $\alpha_i(x)$ is the splat opacity at pixel x and Ω_i is the set of pixels influenced by \mathcal{G}_i . This measures how the photometric error increases as the Gaussian’s opacity is reduced (e.g. how important the Gaussian is for reconstruction accuracy).

We generalize this to semantic-guided pruning by also including the gradient of the feature reconstruction loss:

$$\psi_i = \sum_{x \in \Omega_i} \left(\lambda_c \left| \frac{\partial \mathcal{L}_{\text{rgb}}}{\partial \alpha_i(x)} \right| + \lambda_f \left| \frac{\partial \mathcal{L}_{\text{feat}}}{\partial \alpha_i(x)} \right| \right),$$

where: λ_c and λ_f balance color and feature importance and $\mathcal{L}_{\text{feat}} = \|\hat{F} - F^{\text{obs}}\|_1$ is the feature supervision loss. Gaussians with low ψ_i contribute negligibly to appearance and semantics, making them ideal candidates for removal.

At each refinement round (triggered whenever a new tracking or mapping keyframe is added) we compute all ψ_i and prune the lowest-scoring Gaussians in the p percentile:

$$\mathcal{G}' = \{\mathcal{G}_i \mid \psi_i > \text{Percentile}(\psi, p)\}.$$

To preserve tracking robustness, we use a conservative removal rate during tracking keyframes ($p = 10\%$) and a more aggressive threshold during mapping keyframes ($p = 30\%$). This prevents excessive deletion of potential correspondences, while still keeping the map size bounded.

This strategy ensures that the retained Gaussians are those most supported by semantic gradients rather than only photometric intensity, which improves long-term geometric stability and reduces drift in low-texture regions. At the end of a refinement round we additionally perform a standard 3DGS pruning of Gaussians that are too large or whose opacity is too low.

4.9. Post-trajectory refinement

While our system maps in real time, Gaussians inserted near the end of the trajectory receive fewer updates than earlier ones. After the final pose graph is fixed, we perform an optional offline refinement pass to uniformly update all Gaussians using all keyframes. We first recompute the 3D distance filter for the full map, ensuring consistent scale and opacity regularisation across the scene, and then run a small number of additional optimisation steps. This global sweep corrects minor inconsistencies accumulated during online training and improves fine-scale geometry and feature consistency, without affecting the real-time performance of the SLAM pipeline. We report results with and without this final optimisation stage. As seen in the experiments it adds around one extra minute of training to the overall time, but raises the map reconstruction accuracy greatly.

5. Experiments

We evaluate our approach on two complementary SLAM benchmarks. The Replica dataset [45] which offers photorealistic, noise-free frames rendered from virtual indoor scenes, while the TUM RGB-D dataset [46] consists of hand-captured sequences characterized by sensor noise, motion blur, and frequent depth dropouts. Testing on both allows us to assess performance under idealized conditions and in the presence of real-world artifacts. All experiments are conducted on an Intel Core i9-10900K CPU (32 GB RAM) and an NVIDIA RTX 3090 GPU (24 GB VRAM).

We report the metrics: **Tracking accuracy** (Absolute Trajectory Error (ATE) RMSE), **Novel-view reconstruction** (PSNR, SSIM, and LPIPS on held-out frames), **Depth quality** (L_1 error, precision, recall, and F1-score with respect to ground-truth depth), **Semantic accuracy** (mean Intersection-over-Union (mIoU) and pixel-wise accuracy of segmentations performed on decoded feature maps of held-out frames), **Runtime** (completion in minutes, including tracking and mapping).

We compare our method with three classes of approaches: **RGB and RGB-D NVS SLAM** (Point-SLAM [43], SplatAM [18], MonoGS, Photo-SLAM, and GS-ICP SLAM [13]), **Closed set Semantic SLAM** (GS-SLAM [50], NIDS-SLAM [14], SGS-SLAM [25], SNI-SLAM [56], NEDS-SLAM [16], SemGauss-SLAM [55], GS3SLAM [24]), **Open set semantic SLAM** (To our knowledge only OVO-SLAM [31] for this task), **Offline feature-distilled 3DGS methods without real-time constraints** (Feature-3DGS [53], GS-Grouping [51], LangSplat [38] and LERF [20]). These methods are trained offline and use full-sequence batch optimization, but we include them to measure the performance gap between online and offline feature distillation.

Category	Method	ATE \downarrow	PSNR \uparrow	SSIM \uparrow	LPIPS \downarrow	L1 Depth (cm) \downarrow	T. Time (mins) \downarrow
Visual SLAM	Point-SLAM [43]	0.46	29.43	0.935	0.235	0.44	144.92
	SplatAM [18]	0.35	33.91	0.969	0.097	0.72	238.09
	GS-SLAM [50]	0.50	34.27	0.975	0.082	1.16	4.01
	LoopSplat [54]	0.26	36.33	0.981	0.112	0.62	163.00
	MonoGS	0.58	36.70	0.960	0.064	1.10	200.75
	Photo-SLAM [15]	0.44	34.13	0.970	0.099	2.50	1.45
Sem.SLAM methods	CartGS [10]	0.48	34.64	0.970	0.101	2.30	1.45
	GS-ICP-SLAM [13]	0.16	38.86	0.970	0.049	4.54	1.11
	SNI-SLAM [56]	0.46	29.43	0.935	0.235	0.87	54.64
	SemGauss-SLAM [55]	0.38	34.83	0.978	0.069	0.53	140.90
	GS3SLAM [24]	0.37	36.26	0.989	0.052	0.62	152.40
	Ours	0.15	41.22	0.986	0.046	0.73	4.44
	Ours+refine	0.15	42.52	0.989	0.040	0.42	5.14

Table 1. Camera tracking and reconstruction on Replica [45] (average over 8 scenes).

5.1. Tracking and Reconstruction Accuracy

Tables 1 and 2 present results on the synthetic Replica [45] and TUM-RGBD [46] datasets respectively. For Replica, our method achieves SOTA tracking accuracy across all evaluated scenes (see supplementary for the per-scene breakdown), consistently outperforming coupled Gaussian SLAM

Method	ATE \downarrow	PSNR \uparrow	SSIM \uparrow	LPIPS \downarrow	T. Time (mins) \downarrow
Photo-SLAM [15]	0.26	18.39	0.647	0.221	4.4
CartGS [10]	0.27	18.55	0.677	0.216	4.2
SplaTAM [18]	5.50	22.77	0.867	0.173	210.2
MonoGS [32]	1.48	18.60	0.751	0.199	130.2
GS-ICP-SLAM [13]	2.64	18.32	0.634	0.246	3.6
Ours	2.05	18.82	0.653	0.190	24.9
Ours+refine	2.05	19.22	0.683	0.187	26.9

Table 2. Camera tracking and reconstruction on TUM [46] (average over 3 scenes).

systems such as the baseline method GS-ICP SLAM [13] and the decoupled methods Photo-SLAM [15]/CartGS[10]. This improvement stems from the combination of multi-layered semantically informed feature correspondences, camera-plane depth and normal estimation, and a compact but expressive Gaussian representation. Unlike purely geometric methods, our tracking is guided not only by 3D structure but also by the high-level semantic features embedded in our model, allowing correspondences to remain stable in low-texture or repetitive regions.

These gains are achieved while running in real time at approximately 5 FPS, without relying on precomputed semantic masks, global bundle adjustment, or loop-closure optimization. Competing approaches that match or surpass our ATE, such as ORB-SLAM3 or loop-closure-based systems like LoopSplat [54], generally require pose graph optimization over the entire sequence and therefore compromise real-time performance.

On the real-world TUM RGB-D dataset [46], our method also achieves comparably low trajectory drift to existing coupled Gaussian-map SLAM systems. Decoupled methods like Photo-SLAM/CartGS achieve a lower ATE but provide lower quality mapping with no semantic understanding. Learned PGO methods succeed in this task but these methods are more than 7 times slower than our approach without providing improved visual results or any semantic segmentation capabilities. The baseline, GS-ICP-SLAM, when evaluated without a depth mask yields very noisy gaussians with poorly localised edges. Although fast, this method suffers in datasets where the quality of depth is poor. This is evident from the significant performance drop between Replica and TUM. In contrast, our method offers a more robust scene representation with excellent reconstruction quality, while still operating online. Comparative novel view reconstructions are shown in Figure 3 highlighting our systems higher level of detail and the absence of floater artifacts.

5.2. Novel-View Open-Set Segmentation

To assess open-set generalization, we integrate our 3D feature fields with open-vocabulary queries via GroundingDINO (see supplementary materials). we compare against offline distillation-based 3DGS models: Fea-



Figure 3. Qualitative comparison of novel-views Replica-office0.

ture3DGS [53], LERF [20], and LangSplat [38]. These methods require full-scene training and pre-extracted 2D features and do not run in real time. For fairness, we provide our SLAM keyframes and ground-truth poses, and train with the authors' default settings for an equal number of iterations. We omit prior semantic SLAM methods that rely on ground-truth label inputs and pre-determined class labels, as these cannot be compared like-for-like on the open-set segmentation task.

Table 3 shows that **FeatureSLAM** matches or exceeds all baselines in zero-shot, novel-view segmentation while also running fully online. The only offline technique that performs on par with FeatureSLAM is LERF, which does well in pixel wise segmentation accuracy (+5%). However, the MIoU score of LERF is significantly lower (-15%). Importantly, our training is approximately $\sim 10\times$ shorter than the next fastest method, and unlike some baselines, requires no dataset preprocessing for masks or CLIP embeddings.

Method	Backbone	MIoU, %	mAcc, %	Training Time
LERF [20]	NeRF+CLIP	31.2	60.7	45 min
LangSplat[38]	3DGS+CLIP	24.7	42.0	180 min
Feature3DGS[53]	3DGS+LSeg	39.9	52.1	150 min
OVO-G.-SLAM[31]	3DGS+CLIP	22.3	41.1	138 min
FeatureSLAM	3DGS+GSAM2	46.3	55.3	5.4 min

Table 3. Comparison of segmentation results on Replica dataset including offline and online (with preprocessing) methods.

6. Conclusion

This paper presented FeatureSLAM, a coupled 3DGS SLAM method capable of operating online in real-time, with no preprocessing required. Our novel, tracking and mapping methodology, provides competitive scene fidelity while enabling open set segmentation capabilities rivalling offline methods that use extensive preprocessing and ground truth poses. Our real-world tests show promise for downstream tasks that current SLAM systems don't support. Future work will stabilize long-term tracking, by performing loop closure with the embedded features.

References

[1] Paul J Besl and Neil D McKay. Method for registration of 3-d shapes. In *Sensor fusion IV: control paradigms and data structures*, pages 586–606. Spie, 1992. 2

[2] Carlos Campos, Richard Elvira, Juan J Gómez Rodríguez, José MM Montiel, and Juan D Tardós. Orb-slam3: An accurate open-source library for visual, visual–inertial, and multimap slam. *IEEE Transactions on Robotics*, 37(6):1874–1890, 2021. 2

[3] X. Chen, A. Milioto, E. Palazzolo, P. Giguère, J. Behley, and C. Stachniss. SuMa++: Efficient LiDAR-based Semantic SLAM. In *Proceedings of the IEEE/RSJ Int. Conf. on Intelligent Robots and Systems (IROS)*, pages 4530–4537, 2019. 2

[4] Ho Kei Cheng, Seoung Wug Oh, Brian Price, Alexander Schwing, and Joon-Young Lee. Tracking anything with de-coupled video segmentation. In *ICCV*, 2023. 2

[5] Dmitry Chetverikov, Dmitry Svirko, Dmitry Stepanov, and Pavel Krsek. The trimmed iterative closest point algorithm. In *2002 International Conference on Pattern Recognition*, pages 545–548. IEEE, 2002. 2

[6] Chi-Ming Chung, Yang-Che Tseng, Ya-Ching Hsu, Xiang-Qian Shi, Yun-Hung Hua, Jia-Fong Yeh, Wen-Chin Chen, Yi-Ting Chen, and Winston H Hsu. Orbeez-slam: A real-time monocular visual slam with orb features and nerf-realized mapping. In *2023 IEEE International Conference on Robotics and Automation (ICRA)*, pages 9400–9406. IEEE, 2023. 2

[7] Jiaming Cui, Jiming Chen, and Liang Li. Sage-icp: Semantic information-assisted icp, 2024. 2

[8] Angela Dai, Matthias Nießner, Michael Zollhöfer, Shahram Izadi, and Christian Theobalt. Bundlefusion: Real-time globally consistent 3d reconstruction using on-the-fly surface reintegration. *ACM Transactions on Graphics (ToG)*, 36(4):1, 2017. 2

[9] Alexey Dosovitskiy, Lucas Beyer, Alexander Kolesnikov, Dirk Weissenborn, Xiaohua Zhai, Thomas Unterthiner, Mostafa Dehghani, Matthias Minderer, Georg Heigold, Sylvain Gelly, Jakob Uszkoreit, and Neil Houlsby. An image is worth 16x16 words: Transformers for image recognition at scale. In *International Conference on Learning Representations*, 2021. 1

[10] Dapeng Feng, Zhiqiang Chen, Yizhen Yin, Shipeng Zhong, Yuhua Qi, and Hongbo Chen. Cartgs: Computational alignment for real-time gaussian splatting slam, 2024. 6, 7, 8, 2, 4

[11] Giorgio Grisetti, Rainer Kümmerle, Cyrill Stachniss, and Wolfram Burgard. A tutorial on graph-based slam. *IEEE Intelligent Transportation Systems Magazine*, 2(4):31–43, 2010. 2

[12] T. Guadagnino, B. Mersch, S. Gupta, I. Vizzo, G. Grisetti, and C. Stachniss. KISS-SLAM: A Simple, Robust, and Accurate 3D LiDAR SLAM System With Enhanced Generalization Capabilities. *arXiv preprint*, arXiv:2503.12660, 2025. 2

[13] Seongbo Ha, Jiung Yeon, and Hyeonwoo Yu. Rgbd gs-icp slam. In *Computer Vision – ECCV 2024: 18th European Conference, Milan, Italy, September 29–October 4, 2024, Proceedings, Part XXXVI*, page 180–197, Berlin, Heidelberg, 2024. Springer-Verlag. 2, 4, 7, 8

[14] Yasaman Haghighi, Suryansh Kumar, Jean-Philippe Thiran, and Luc Van Gool. Neural implicit dense semantic slam. *arXiv preprint arXiv:2304.14560*, 2023. 7

[15] Huajian Huang, Longwei Li, Cheng Hui, and Sai-Kit Yeung. Photo-slam: Real-time simultaneous localization and photo-realistic mapping for monocular, stereo, and rgbd cameras. In *Proceedings of the IEEE/CVF Conference on Computer Vision and Pattern Recognition*, 2024. 2, 7, 8, 4

[16] Yiming Ji, Yang Liu, Guanghu Xie, Boyu Ma, Zongwu Xie, and Hong Liu. Neds-slam: A neural explicit dense semantic slam framework using 3d gaussian splatting. *IEEE Robotics and Automation Letters*, 9(10):8778–8785, 2024. 1, 2, 7

[17] Mohammad Mahdi Johari, Camilla Carta, and François Fleuret. Eslam: Efficient dense slam system based on hybrid representation of signed distance fields. In *Proceedings of the IEEE/CVF Conference on Computer Vision and Pattern Recognition*, pages 17408–17419, 2023. 2

[18] Nikhil Keetha, Jay Karhade, Krishna Murthy Jatavallabhula, Gengshan Yang, Sebastian Scherer, Deva Ramanan, and Jonathon Luiten. Splatam: Splat, track & map 3d gaussians for dense rgbd slam. *arXiv preprint arXiv:2312.02126*, 2023. 2, 7, 8, 4

[19] Bernhard Kerbl, Georgios Kopanas, Thomas Leimkühler, and George Drettakis. 3d gaussian splatting for real-time radiance field rendering. *ACM Transactions on Graphics*, 42(4):1–14, 2023. 1

[20] Justin* Kerr, Chung Min* Kim, Ken Goldberg, Angjoo Kanazawa, and Matthew Tancik. Lerf: Language embedded radiance fields. In *International Conference on Computer Vision (ICCV)*, 2023. 7, 8

[21] Alexander Kirillov, Eric Mintun, Nikhila Ravi, Hanzi Mao, Chloe Rolland, Laura Gustafson, Tete Xiao, Spencer Whitehead, Alexander C. Berg, Wan-Yen Lo, Piotr Dollár, and Ross Girshick. Segment anything. *arXiv:2304.02643*, 2023. 2

[22] Xin Kong, Shikun Liu, Marwan Taher, and Andrew J Davison. vmap: Vectorised object mapping for neural field slam. In *Proceedings of the IEEE/CVF Conference on Computer Vision and Pattern Recognition*, pages 952–961, 2023. 2

[23] Boyi Li, Kilian Q Weinberger, Serge Belongie, Vladlen Koltun, and Rene Ranftl. Language-driven semantic segmentation. In *International Conference on Learning Representations*, 2022. 1, 2

[24] Linfei Li, Lin Zhang, Zhong Wang, and Ying Shen. Gs3lam: Gaussian semantic splatting slam. In *Proceedings of the 32nd ACM International Conference on Multimedia*, page 3019–3027, New York, NY, USA, 2024. Association for Computing Machinery. 1, 2, 7

[25] Mingrui Li, Shuhong Liu, Heng Zhou, Guohao Zhu, Na Cheng, Tianchen Deng, and Hongyu Wang. Sgs-slam: Semantic gaussian splatting for neural dense slam. In *European Conference on Computer Vision*, pages 163–179. Springer, 2024. 7

[26] Xinyi Li and Haibin Ling. Pogo-net: Pose graph optimization with graph neural networks. In *Proceedings of the IEEE/CVF International Conference on Computer Vision (ICCV)*, pages 5875–5885, Montreal, QC, Canada, 2021. 2

[27] Shilong Liu, Zhaoyang Zeng, Tianhe Ren, Feng Li, Hao Zhang, Jie Yang, Chunyuan Li, Jianwei Yang, Hang Su, Jun Zhu, et al. Grounding dino: Marrying dino with grounded pre-training for open-set object detection. *arXiv preprint arXiv:2303.05499*, 2023. 2

[28] Kok-Lim Low. Linear least-squares optimization for point-to-plane icp surface registration. *Chapel Hill, University of North Carolina*, 4(10):1–3, 2004. 2

[29] Saswat Bhajayoti Mallick, Rahul Goel, Bernhard Kerbl, Markus Steinberger, Francisco Vicente Carrasco, and Fernando De La Torre. Taming 3dgs: High-quality radiance fields with limited resources. In *SIGGRAPH Asia 2024 Conference Papers*, New York, NY, USA, 2024. Association for Computing Machinery. 5

[30] Angelos Mallios, Pere Ridao, David Ribas, and Emili Hernández. Scan matching slam in underwater environments. *Autonomous Robots*, 36:181–198, 2014. 2

[31] Tomas Berriel Martins, Martin R. Oswald, and Javier Civera. Open-vocabulary online semantic mapping for slam. *IEEE Robotics and Automation Letters*, 2025. 7, 8

[32] Hidenobu Matsuki, Riku Murai, Paul H. J. Kelly, and Andrew J. Davison. Gaussian Splatting SLAM. In *Proceedings of the IEEE/CVF Conference on Computer Vision and Pattern Recognition*, 2024. 2, 8, 4

[33] Ben Mildenhall, Pratul P. Srinivasan, Matthew Tancik, Jonathan T. Barron, Ravi Ramamoorthi, and Ren Ng. Nerf: Representing scenes as neural radiance fields for view synthesis. In *Computer Vision – ECCV 2020*, pages 405–421. Springer, 2020. 1, 2

[34] Richard A Newcombe, Shahram Izadi, Otmar Hilliges, David Molyneaux, David Kim, Andrew J Davison, Pushmeet Kohi, Jamie Shotton, Steve Hodges, and Andrew Fitzgibbon. Kinectfusion: Real-time dense surface mapping and tracking. In *2011 10th IEEE international symposium on mixed and augmented reality*, pages 127–136. Ieee, 2011. 2

[35] Juan Nieto, Tim Bailey, and Eduardo Nebot. Recursive scan-matching slam. *Robotics and Autonomous systems*, 55(1):39–49, 2007. 2

[36] Steven A Parkison, Lu Gan, Maani Ghaffari Jadidi, and Ryan M. Eustice. Semantic iterative closest point through expectation-maximization. In *Proceedings of the British Machine Vision Conference*, pages 1–17, Newcastle, UK, 2018. 2

[37] Victor Adrian Prisacariu, Olaf Kähler, Stuart Golodetz, Michael Sapienza, Tommaso Cavallari, Philip HS Torr, and David W Murray. Infinitam v3: A framework for large-scale 3d reconstruction with loop closure. *arXiv preprint arXiv:1708.00783*, 2017. 2

[38] Minghan Qin, Wanhua Li, Jiawei Zhou, Haoqian Wang, and Hanspeter Pfister. Langsplat: 3d language gaussian splatting. *arXiv preprint arXiv:2312.16084*, 2023. 2, 7, 8

[39] Alec Radford, Jong Wook Kim, Chris Hallacy, Aditya Ramesh, Gabriel Goh, Sandhini Agarwal, Girish Sastry, Amanda Askell, Pamela Mishkin, Jack Clark, Gretchen Krueger, and Ilya Sutskever. Learning transferable visual models from natural language supervision. In *Proceedings of the 38th International Conference on Machine Learning*, pages 8748–8763. PMLR, 2021. 1

[40] Nikhila Ravi, Valentin Gabeur, Yen-Cheng Hu, Ronghang Hu, et al. Sam 2.0: Segment anything in images and videos. *arXiv preprint arXiv:2408.00714*, 2024. 1, 2

[41] Tianhe Ren, Qing Jiang, Shilong Liu, Zhaoyang Zeng, Wenlong Liu, Han Gao, Hongjie Huang, Zhengyu Ma, Xiaoke Jiang, Yihao Chen, Yuda Xiong, Hao Zhang, Feng Li, Peijun Tang, Kent Yu, and Lei Zhang. Grounding dino 1.5: Advance the “edge” of open-set object detection, 2024. 2

[42] Tianhe Ren, Shilong Liu, Ailing Zeng, Jing Lin, Kunchang Li, He Cao, Jiayu Chen, Xinyu Huang, Yukang Chen, Feng Yan, Zhaoyang Zeng, Hao Zhang, Feng Li, Jie Yang, Hongyang Li, Qing Jiang, and Lei Zhang. Grounded sam: Assembling open-world models for diverse visual tasks, 2024. 2

[43] Erik Sandström, Yue Li, Luc Van Gool, and Martin R Oswald. Point-slam: Dense neural point cloud-based slam. In *Proceedings of the IEEE/CVF International Conference on Computer Vision*, pages 18433–18444, 2023. 2, 7

[44] Aleksandr Segal, Dirk Haehnel, and Sebastian Thrun. Generalized-icp. In *Robotics: science and systems*, page 435. Seattle, WA, 2009. 2

[45] Julian Straub, Thomas Whelan, Lingni Ma, Yufan Chen, Erik Wijmans, Simon Green, Jakob J Engel, Raul Mur-Artal, Carl Ren, Shobhit Verma, et al. The replica dataset: A digital replica of indoor spaces. *arXiv preprint arXiv:1906.05797*, 2019. 7, 2

[46] Jürgen Sturm, Nikolas Engelhard, Felix Endres, Wolfram Burgard, and Daniel Cremers. A benchmark for the evaluation of rgbd-slam systems. In *2012 IEEE/RSJ international conference on intelligent robots and systems*, pages 573–580. IEEE, 2012. 7, 8, 4

[47] Edgar Sucar, Shikun Liu, Joseph Ortiz, and Andrew J Davison. imap: Implicit mapping and positioning in real-time. In *Proceedings of the IEEE/CVF International Conference on Computer Vision*, pages 6229–6238, 2021. 2

[48] Ignacio Vizzo, Tiziano Guadagnino, Benedikt Mersch, Louis Wiesmann, Jens Behley, and Cyrill Stachniss. KISS-ICP: In Defense of Point-to-Point ICP – Simple, Accurate, and Robust Registration If Done the Right Way. *IEEE Robotics and Automation Letters (RA-L)*, 8(2):1029–1036, 2023. 2

[49] Jay Wong, Vincent Kee, Tiffany Le, Syler Wagner, Gian-Luca Mariottini, Abraham Schneider, Lei Hamilton, Rahul Chipalkatty, Mitchell Hebert, David Johnson, Jimmy Wu, Bolei Zhou, and Antonio Torralba. Segicp: Integrated deep semantic segmentation and pose estimation. 2017. 2

[50] Chi Yan, Delin Qu, Dong Wang, Dan Xu, Zhigang Wang, Bin Zhao, and Xuelong Li. Gs-slam: Dense visual slam with 3d gaussian splatting. *arXiv preprint arXiv:2311.11700*, 2023. 7

[51] Mingqiao Ye, Martin Danelljan, Fisher Yu, and Lei Ke. Gaussian grouping: Segment and edit anything in 3d scenes. In *ECCV*, 2024. 2, 7

[52] Baowen Zhang, Chuan Fang, Rakesh Shrestha, Yixun Liang, Xiaoxiao Long, and Ping Tan. Rade-gs: Rasterizing depth in gaussian splatting. *arXiv preprint*, 2024. 4

[53] Shijie Zhou, Haoran Chang, Sicheng Jiang, Zhiwen Fan, Zehao Zhu, Dejia Xu, Pradyumna Chari, Suya You, Zhangyang Wang, and Achuta Kadambi. Feature 3dgs: Supercharging

3d gaussian splatting to enable distilled feature fields. In *Proceedings of the IEEE/CVF Conference on Computer Vision and Pattern Recognition*, pages 21676–21685, 2024. [1](#), [2](#), [7](#), [8](#)

[54] Liyuan Zhu, Yue Li, Erik Sandström, Shengyu Huang, Konrad Schindler, and Iro Armeni. Loopsplat: Loop closure by registering 3d gaussian splats. In *International Conference on 3D Vision (3DV)*, 2025. [7](#), [8](#), [2](#)

[55] Siting Zhu, Renjie Qin, Guangming Wang, Jiuming Liu, and Hesheng Wang. Semgauss-slam: Dense semantic gaussian splatting slam. *arXiv preprint arXiv:2403.07494*, 2024. [2](#), [7](#)

[56] Siting Zhu, Guangming Wang, Hermann Blum, Jiuming Liu, Liang Song, Marc Pollefeys, and Hesheng Wang. Sni-slam: Semantic neural implicit slam. In *Proceedings of the IEEE/CVF Conference on Computer Vision and Pattern Recognition*, pages 21167–21177, 2024. [1](#), [7](#)

[57] Zihan Zhu, Songyou Peng, Viktor Larsson, Weiwei Xu, Hujun Bao, Zhaopeng Cui, Martin R Oswald, and Marc Pollefeys. Nice-slam: Neural implicit scalable encoding for slam. In *Proceedings of the IEEE/CVF Conference on Computer Vision and Pattern Recognition*, pages 12786–12796, 2022. [2](#)

FeatureSLAM: Feature-enriched 3D gaussian splatting SLAM in real time

Supplementary Material

In this supplementary materials document, we present a range of deeper evaluations for the FeatureSLAM method. This includes more nuanced details about the performance than could be fit into the main paper, alongside additional ablations and demonstrations of the new types of downstream application enabled by FeatureSLAM.

We first report per-scene quantitative tracking and reconstruction results on Replica and TUM-RGBD, complementing the aggregated metrics in the main paper. We then provide additional qualitative visualizations of the prompt-less segmentation capability enabled by SAM2 features, as well as examples of language-driven queries via GroundingDINO. Finally, we include a set of ablation studies analysing our pruning strategy, post-trajectory refinement, and feature latent space design, together with further qualitative RGB renderings.

7. Live demo demonstration

We provide an accompanying video demonstrating FeatureSLAM running live on RGB-D input (realsense i435). The demo shows the real-time evolution of the Gaussian map, together with the current camera pose and rendered novel views. As the sensor moves, our feature-guided GICP tracker maintains stable trajectories while the map is densified and refined online. We also visualise the decoded feature maps and segmentation overlays to highlight how SAM2 features remain temporally consistent and support interactive querying during operation, rather than only in an offline post-processing stage. Please see Fig.4 for example screenshots from the video.

8. Per-scene quantitative results for Replica

Table 4 reports per-scene tracking and reconstruction metrics on the Replica benchmark. Across the three room and five office sequences, our method is competitive with or better than geometry-focused baselines such as GS-ICP-SLAM in terms of trajectory error, while approaching or surpassing photometric methods (e.g. MonoGS, Loop-Splat) in reconstruction quality. This supports the claim from the main paper that coupling feature-guided tracking with feature-augmented mapping yields both stable trajectories and high-fidelity maps, rather than trading one for the other. It also demonstrates that these gains are general and consistent across scenes. It is also noteworthy that the refined variant (*Ours+refine*) further improves map fidelity with only a small additional offline optimisation pass, primarily boosting PSNR and LPIPS while leaving ATE largely unchanged.

We report the corresponding per-sequence results on

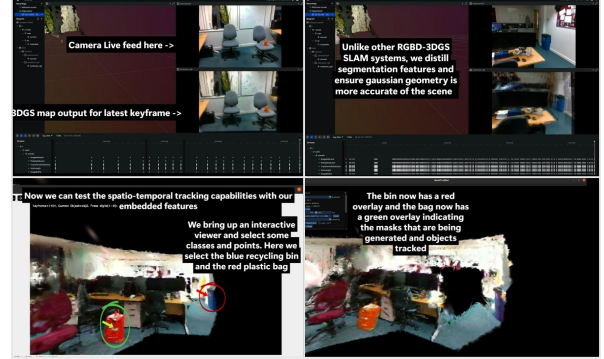


Figure 4. Screenshots from the live demonstration and free camera viewer

TUM-RGBD in Table 5. Compared to the synthetic Replica scenes, these real-world sequences contain sensor noise, motion blur and depth dropouts. FeatureSLAM maintains competitive ATE while delivering comparable or better reconstruction quality to existing coupled Gaussian-map methods, illustrating that the proposed feature-guided tracking and depth-normal regularisation remain effective under real sensor artefacts.

9. Prompt-less segmentation visualizations

In this section we qualitatively assess the segmentation quality obtained directly from the SAM2 feature encoder, without any language or point prompts. For each scene, we render our latent feature cloud and decode the per-pixel features from our learned latent space, applying the SAM2 decoder heads to obtain dense masks. Figures 5–7 overlay these masks on the ground-truth RGB frames.

The results show that the prompt-less masks already exhibit coherent object extents and sharp boundaries, even for thin structures and texture-poor regions. Importantly, these segmentations are produced from the feature-enriched 3DGS map, rather than from raw RGB frames, demonstrating that the compact latent representation preserves sufficient semantics for downstream segmentation without additional supervision. We can also note that despite operating as an online SLAM system, our segmentation results are of similar quality, to those of the offline F3DGS method and the non-novel-view SAM2 results.

Methods	Metrics	R0	R1	R2	Of0	Of1	Of2	Of3	Of4	Avg.
Photo-SLAM [15]	ATE ↓	0.30	0.33	0.18	0.45	0.35	1.13	0.37	0.44	0.46
	PSNR [dB] ↑	27.29	29.87	27.37	31.61	31.96	30.43	29.33	27.87	29.43
	SSIM ↑	0.910	0.921	0.951	0.967	0.923	0.956	0.927	0.956	0.935
	LPIPS ↓	0.269	0.255	0.168	0.148	0.185	0.175	0.164	0.193	0.235
CartGS [10]	ATE ↓	0.33	0.31	0.16	0.42	0.39	1.06	0.38	0.44	0.46
	PSNR [dB] ↑	27.89	30.87	27.87	32.81	32.66	31.78	30.33	30.97	29.43
	SSIM ↑	0.930	0.929	0.971	0.967	0.923	0.956	0.927	0.956	0.935
	LPIPS ↓	0.269	0.255	0.168	0.148	0.185	0.175	0.164	0.193	0.235
Point-SLAM [43]	ATE ↓	0.61	0.41	0.37	0.38	0.48	0.54	0.69	0.72	0.53
	PSNR [dB] ↑	32.40	34.08	35.50	38.26	39.16	33.99	33.48	33.49	35.05
	SSIM ↑	0.974	0.977	0.982	0.983	0.986	0.960	0.960	0.979	0.975
	LPIPS ↓	0.113	0.116	0.111	0.100	0.118	0.156	0.132	0.142	0.124
SplaTAM [18]	ATE ↓	0.31	0.40	0.29	0.47	0.27	0.29	0.32	0.72	0.36
	PSNR [dB] ↑	32.86	33.89	35.25	38.26	39.17	31.97	29.70	31.80	34.11
	SSIM ↑	0.980	0.971	0.980	0.980	0.980	0.970	0.950	0.950	0.970
	LPIPS ↓	0.070	0.100	0.080	0.090	0.090	0.100	0.120	0.150	0.100
LoopSplat [54]	ATE ↓	0.28	0.22	0.17	0.22	0.16	0.49	0.20	0.30	0.26
	PSNR [dB] ↑	33.07	35.32	36.16	40.82	40.21	34.67	35.67	37.10	36.63
	SSIM ↑	0.973	0.978	0.985	0.992	0.990	0.985	0.990	0.989	0.985
	LPIPS ↓	0.116	0.122	0.111	0.085	0.123	0.140	0.096	0.106	0.112
MonoGS	ATE ↓	0.33	0.22	0.29	0.36	0.19	0.25	0.12	0.81	0.32
	PSNR [dB] ↑	34.29	35.77	36.79	40.87	40.73	35.22	35.89	34.98	36.81
	SSIM ↑	0.953	0.957	0.965	0.979	0.977	0.961	0.962	0.955	0.964
	LPIPS ↓	0.071	0.078	0.074	0.048	0.052	0.074	0.061	0.092	0.069
GS-ICP-SLAM [13]	ATE ↓	0.20	0.14	0.22	0.21	0.24	0.16	0.16	0.12	0.16
	PSNR [dB] ↑	34.89	37.15	37.89	40.62	41.06	32.69	31.45	38.54	38.86
	SSIM ↑	0.955	0.965	0.970	0.977	0.978	0.965	0.959	0.969	0.970
	LPIPS ↓	0.048	0.041	0.047	0.037	0.039	0.057	0.057	0.045	0.046
SemGauss-SLAM [55]	ATE ↓	0.26	0.42	0.27	0.34	0.17	0.32	0.36	0.49	0.33
	PSNR [dB] ↑	32.55	33.32	35.15	38.39	39.07	32.11	31.60	35.00	34.65
	SSIM ↑	0.979	0.970	0.980	0.989	0.972	0.978	0.972	0.978	0.978
	LPIPS ↓	0.055	0.054	0.045	0.048	0.046	0.069	0.078	0.093	0.061
Ours	ATE ↓	0.14	0.14	0.11	0.18	0.12	0.16	0.16	0.12	0.14
	PSNR [dB] ↑	36.08	39.77	36.46	39.19	39.38	42.60	42.33	38.95	41.22
	SSIM ↑	0.971	0.972	0.980	0.985	0.984	0.974	0.979	0.975	0.986
	LPIPS ↓	0.042	0.043	0.045	0.036	0.036	0.058	0.042	0.041	0.046
Ours+refine	PSNR [dB] ↑	38.06	41.77	38.52	41.29	42.38	43.38	43.01	37.35	42.52
	SSIM ↑	0.986	0.984	0.984	0.989	0.991	0.982	0.981	0.985	0.989
	LPIPS ↓	0.036	0.041	0.041	0.024	0.028	0.037	0.036	0.038	0.040

Table 4. Per-scene camera tracking and reconstruction on Replica [45]. R0–R2 denote room0–2, Of0–Of4 denote office0–4.



Figure 5. Promptless segmentation result with overlay visualisation from GT rgb image.

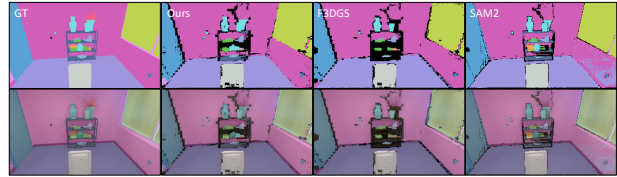


Figure 6. Promptless segmentation result with overlay visualisation from GT rgb image.

10. Grounding-SAM2 integration

To enable language-driven queries, we integrate our 3D feature field with an open-vocabulary grounding model. Con-



Figure 7. Promptless segmentation result with overlay visualisation from GT rgb image.

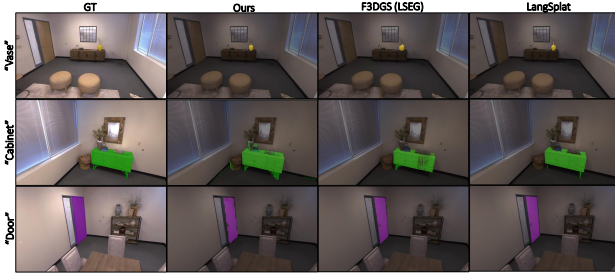


Figure 8. Examples of language prompting used with featureSLAM against Feature3DGS using LSeg and LangSplat.

cretely, we use GroundingDINO to detect 2D regions matching a text query (e.g. “chair”, “monitor on the desk”) on rendered views of the scene. The detected boxes are then passed to the SAM2 decoder, which refines them into high-resolution masks in image space. Finally, these 2D masks are back-projected and accumulated over viewpoints to obtain consistent 3D segments in the Gaussian map.

This pipeline allows FeatureSLAM to answer free-form queries at test time without retraining: language prompts are converted into spatial masks that can be visualised from arbitrary viewpoints or used to filter Gaussians for downstream tasks. Figure 8 illustrates several examples, where different textual prompts activate semantically meaningful subsets of the scene. Compared to label-based semantic SLAM, this approach is not restricted to a fixed ontology and naturally supports compositional or fine-grained queries.

The results demonstrate that our online FeatureSLAM approach can achieve comparable open-set segmentation performance to existing offline 3DGS approaches, with better segment coherence than F3DGS and similar sharp edges to LangSplat.

11. Candidate percentage ablations

We next study the impact of the semantic gradient-based pruning scheme introduced in Sec. 4.8 of the main paper. At each refinement round we remove Gaussians in the lowest p -th percentile of the importance score, and vary p independently for tracking and mapping keyframes. Table 6 reports results when pruning candidates during tracking updates, while Table 7 reports pruning during mapping.

Overall, aggressive pruning (large p) substantially reduces the number of Gaussians but degrades ATE and perceptual quality, as informative but low-gradient splats are removed. Conversely, disabling pruning ($p = 0$) yields slightly better reconstruction metrics but leads to larger maps and slower optimisation. We adopt moderate pruning rates in our main experiments, which preserve tracking robustness while keeping the map size and runtime bounded, matching the qualitative behaviour discussed in the main paper.

12. Post trajectory refinement ablations

Next, we analyse the optional post-trajectory refinement stage described in Sec. 4.9 of the main paper. After fixing the final pose graph, we perform additional optimisation over all Gaussians using all keyframes. The first ablation (Table 8) varies the number of refinement iterations. We observe consistent gains in PSNR and SSIM compared to the no-refinement baseline (0 steps), with diminishing returns beyond a few thousand iterations. In particular, 3k–5k extra steps significantly improve perceptual quality (lower LPIPS) while adding less than a minute of computation.

The second ablation (Table 9) compares different densification strategies during refinement. Classic 3DGS densification, Taming3DGS-style densification, and our MCMC variant all lead to improvements over the no-densification baseline. Classic and MCMC densification yield the best trade-off between PSNR and LPIPS, with only minor differences between them. For simplicity, we use a fixed densification schedule in all main experiments and treat this stage as an optional quality boost that does not affect the real-time nature of the online SLAM pipeline.

13. Latent space feature size ablation

Our feature autoencoder compresses multi-scale SAM2 descriptors into a compact latent embedding attached to each Gaussian. Table 10 evaluates different latent dimensionalities $D \in \{16, 20, 24, 28, 32\}$ on TUM-RGBD. Increasing D generally improves segmentation quality (higher mIoU) and slightly raises PSNR and SSIM, as the autoencoder can retain more fine-grained semantics and local detail. However, very large feature vectors increase memory footprint and slow optimisation.

In practice, we use an intermediate latent size in our main experiments, which provides a good balance between reconstruction quality, segmentation performance, and runtime. This confirms that a relatively low-dimensional feature space is sufficient to preserve most of the semantic information from SAM2 while remaining compatible with real-time SLAM.



Figure 9. RGB rendered result highlighting high level of detail recovered from our method



Figure 10. RGB rendered result highlighting high level of detail recovered from our method

14. Additional visualization results

To complement the quantitative results, we show additional RGB renderings from FeatureSLAM in Figs. 9–11. These examples illustrate that our feature-enriched 3DGS maps recover sharp geometry, fine texture details, and consistent appearance across viewpoints, even in cluttered indoor scenes. The absence of prominent floater artefacts and the crisp object boundaries align with the improvements in depth and normal consistency reported in the main paper.



Figure 11. RGB rendered result highlighting high level of detail recovered from our method

Methods	Metrics	xyz	Desk	office	Avg.
Photo-SLAM [15]	ATE ↓	1.49	0.32	1.72	0.26
	PSNR [dB] ↑	17.58	18.25	19.32	18.39
	SSIM ↑	0.6381	0.6122	0.6965	0.647
	LPIPS ↓	0.2903	0.1902	0.2345	0.221
CartGS [10]	ATE ↓	1.52	0.30	0.90	0.27
	PSNR [dB] ↑	17.78	18.35	19.52	18.55
	SSIM ↑	0.6451	0.6172	0.7265	0.677
	LPIPS ↓	0.2803	0.1982	0.2245	0.216
SplaTAM [18]	ATE ↓	2.81	0.82	6.22	5.50
	PSNR [dB] ↑	21.03	23.11	19.92	22.77
	SSIM ↑	0.87	0.90	0.84	0.867
	LPIPS ↓	0.24	0.21	0.34	0.173
MonoGS [32]	ATE ↓	1.50	1.45	1.50	1.48
	PSNR [dB] ↑	17.31	22.06	23.02	18.60
	SSIM ↑	0.61	0.69	0.62	0.751
	LPIPS ↓	0.38	0.27	0.32	0.199
GS-ICP-SLAM [13]	ATE ↓	3.07	1.79	2.67	2.64
	PSNR [dB] ↑	15.62	18.43	19.20	18.32
	SSIM ↑	0.582	0.611	0.681	0.634
	LPIPS ↓	0.371	0.244	0.211	0.246
Ours	ATE ↓	2.09	1.58	2.48	2.05
	PSNR [dB] ↑	17.75	19.02	19.57	18.82
	SSIM ↑	0.732	0.771	0.776	0.653
	LPIPS ↓	2.429	0.140	0.196	0.190
Ours+refine	PSNR [dB] ↑	18.05	22.02	20.57	18.82
	SSIM ↑	0.732	0.841	0.776	0.653
	LPIPS ↓	0.208	0.131	0.176	0.175

Table 5. Per-scene camera tracking and reconstruction on TUM-RGBD [46]. S1–S3 denote the three evaluated sequences.

Prune %	ATE ↓	PSNR ↑	SSIM ↑	LPIPS ↓
20	2.88	18.02	0.612	0.266
15	2.58	18.22	0.635	0.221
10	2.45	18.44	0.633	0.202
5	2.05	18.82	0.653	0.190
0	2.02	18.81	0.653	0.189

Table 6. Pruning ablation on tracking keyframe points.

Prune %	ATE \downarrow	PSNR \uparrow	SSIM \uparrow	LPIPS \downarrow
40	2.08	18.38	0.632	0.258
30	2.02	18.60	0.651	0.199
20	2.04	18.81	0.867	0.173
10	2.02	18.85	0.653	0.189
0	2.02	18.93	0.655	0.187

Table 7. Pruning ablation on Mapping keyframe points.

Num. iterations	PSNR \uparrow	SSIM \uparrow	LPIPS \downarrow	Ext Time (s)
5k	37.03	0.981	0.034	91
3k	36.25	0.975	0.044	57
1k	35.95	0.967	0.046	18
0	35.35	0.958	0.049	-

Table 8. Refinement Number of training steps ablation study for room0 no densification.

Densification strat	PSNR \uparrow	SSIM \uparrow	LPIPS \downarrow
Classic	38.03	0.991	0.029
Taming	37.89	0.987	0.032
MCMC	38.04	0.990	0.029

Table 9. Refinement Densification strategy ablation study. Using 5k extra steps and two densification steps at 0 and 2k steps of the refinement.

Latent space	PSNR \uparrow	SSIM \uparrow	LPIPS \downarrow	mIoU \downarrow
16	18.72	0.643	0.199	38.7
20	18.56	0.633	0.179	41.1
24	18.82	0.653	0.183	46.3
28	18.92	0.657	0.186	47.2
32	18.89	0.657	0.183	48.1

Table 10. Latent space ablation table on TUM.